Energy Materials

Supplementary Materials

Four-leaf clover triboelectric nanogenerator based on magnetic force separation principle

Shiqin Feng[1], Jielu Lan[1], Jincheng Wu[1], Xinyue Cheng[1], Wei Tang[1], Jiaqi Duan[1], Lingyu Wan[1], Gui Li[1], Guanlin Liu[1,*], Jiyu Wang[2,*]

[1]Center on Nanoenergy Research, Institute of Science and Technology for Carbon Peak & Neutrality, School of Physical Science & Technology, Guangxi University, Nanning 530004, Guangxi, China.
[2]State Key Laboratory of Advanced Electromagnetic Technology, Huazhong University of Science and Technology, Wuhan 430074, Hubei, China.

Correspondence to: Assoc. Prof. Guanlin Liu, Center on Nanoenergy Research, Institute of Science and Technology for Carbon Peak & Neutrality, School of Physical Science & Technology, Guangxi University, Nanning 530004, Guangxi, China. mail: guanlinliu@gxu.edu.cn; Jiyu Wang, State Key Laboratory of Advanced Electromagnetic Technology, Huazhong University of Science and Technology, Wuhan 430074, Hubei, China. E-mail: jiyuwang@hust.edu.cn

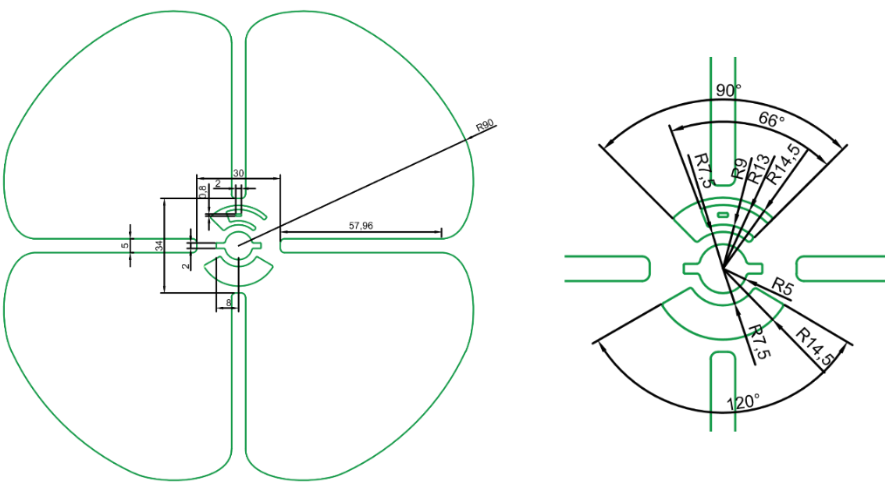

Figure S1. Schematic diagram of the four-leaf clover silicon-manganese steel sheet.

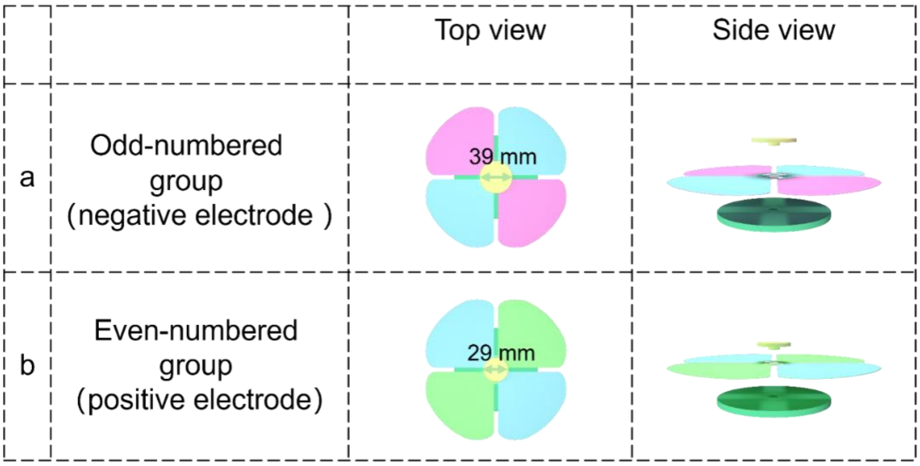

Figure S2. Schematic diagram of film cutting for odd-numbered and even-numbered steel sheet groups of the FL-TENG.

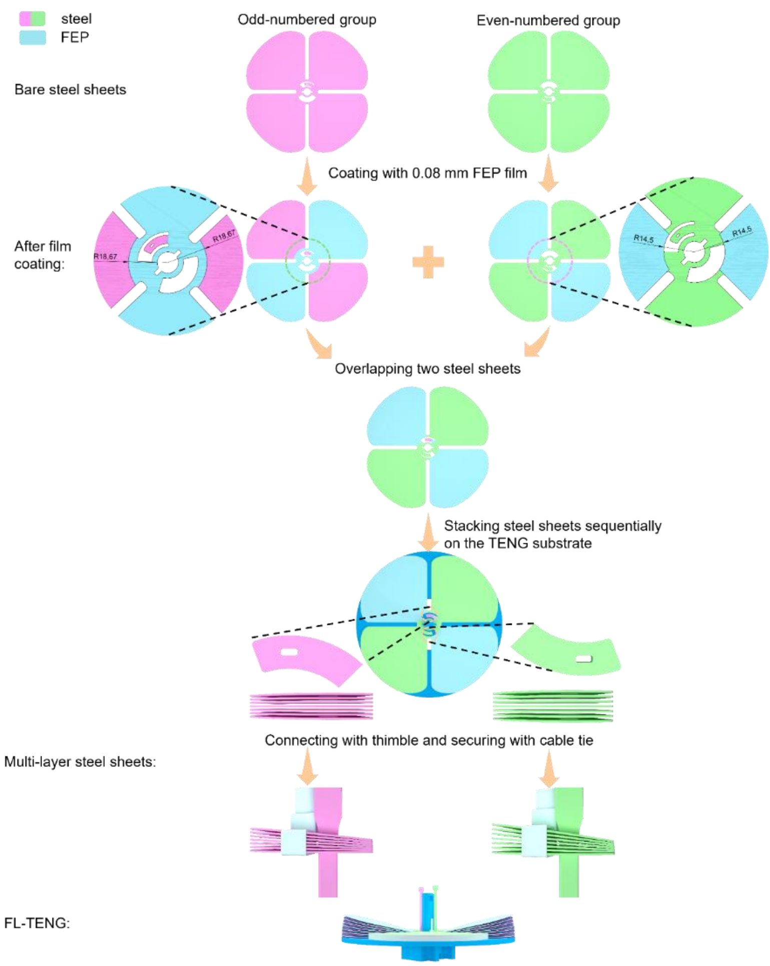

Figure S3. Specific connection method and fabrication process of the FL-TENG.

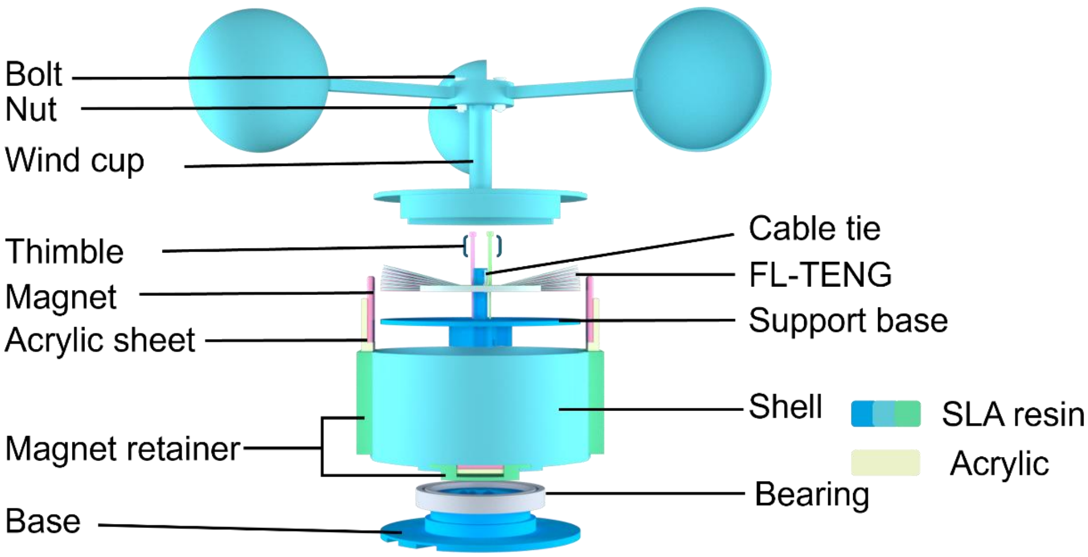

Figure S4. Basic structure of the four-leaf clover triboelectric nanogenerator (FL-TENG) based on the magnetic force separation principle.

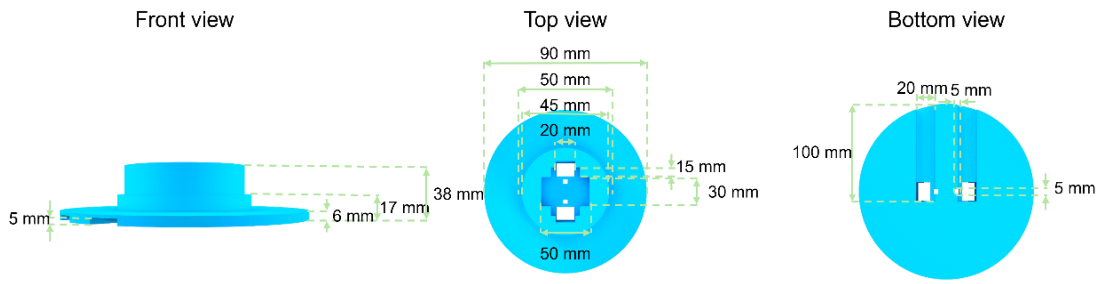

Figure S5. Basic structural parameters and schematic diagrams from different perspectives of the base.

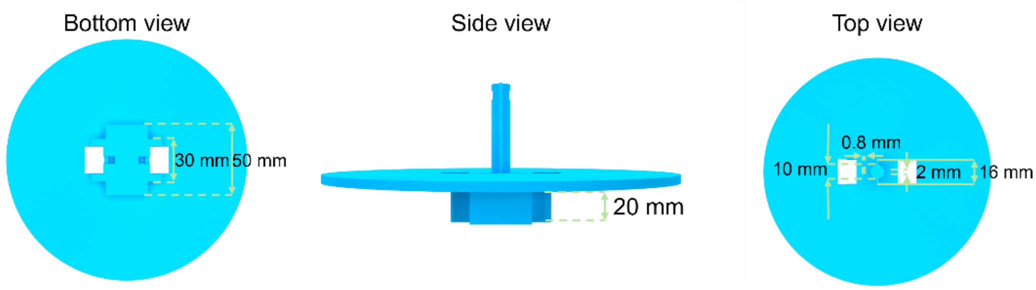

Figure S6. Basic structural parameters and schematic diagrams from different perspectives of the support base.

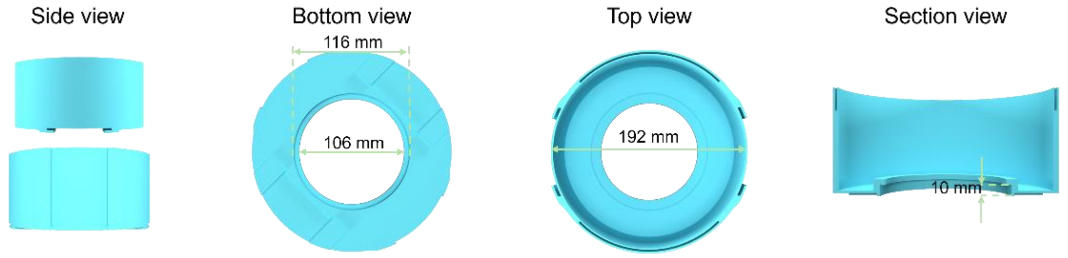

Figure S7. Basic structural parameters and schematic diagrams from different perspectives of the shell.

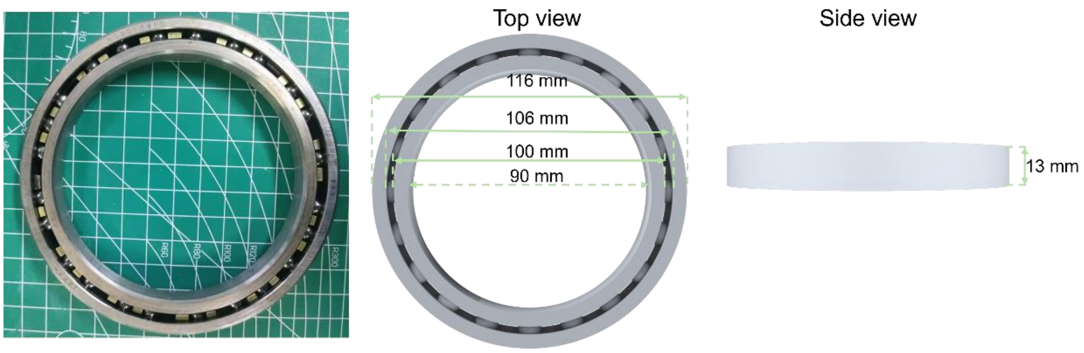

Figure S8. Basic structural parameters and schematic diagrams from different perspectives of the bearing.

Table S1. A comparative summary between FL-TENG and other magnet-assisted TENGs.

Comparison dimension	**Other magnet-assisted TENGs (Ref.[4,38])**	**This work**
Function of magnets	Direct mechanical force providers	Magnetization sources for silicon-manganese steel sheets
Object of magnetic interaction	Between magnets, or between magnets and soft magnetic materials	Between magnetized silicon-manganese steel sheets

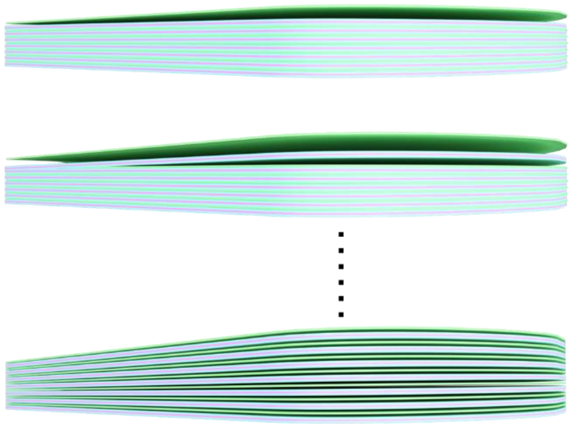

Figure S9. Layer-by-layer separation of multilayer silicon-manganese steel sheets from top to bottom.

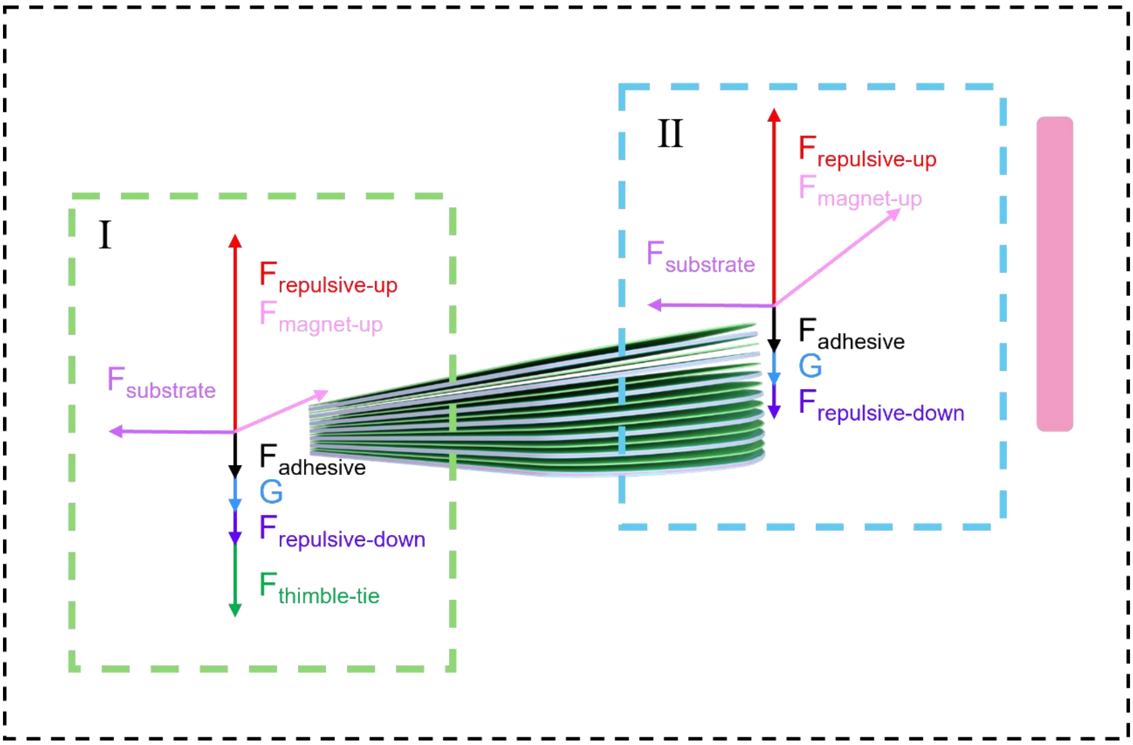

Figure S10. Force analysis comparison of inner and outer regions of the steel sheet. I: The force analysis of the inner central region of the steel sheet. II: The force analysis of the outer edge of the steel sheet.

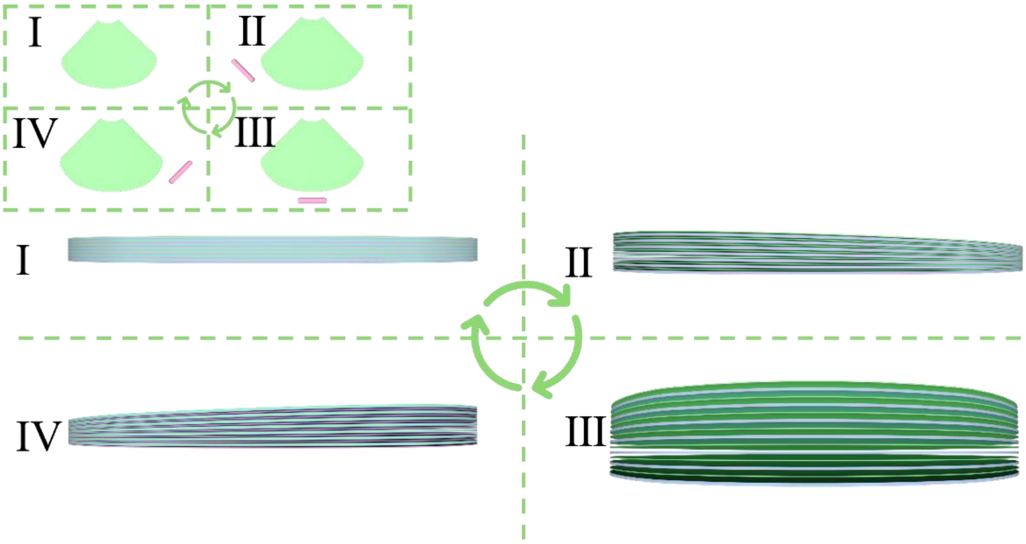

Figure S11. Four working states of one set of friction layers of the FL-TENG during the rotation of the magnet. I: The magnet is far away from the triboelectric layer. II: The magnet gradually approaches the triboelectric layer. III: The magnet is directly facing the triboelectric layer. IV: The magnet gradually moves away from the triboelectric layer.

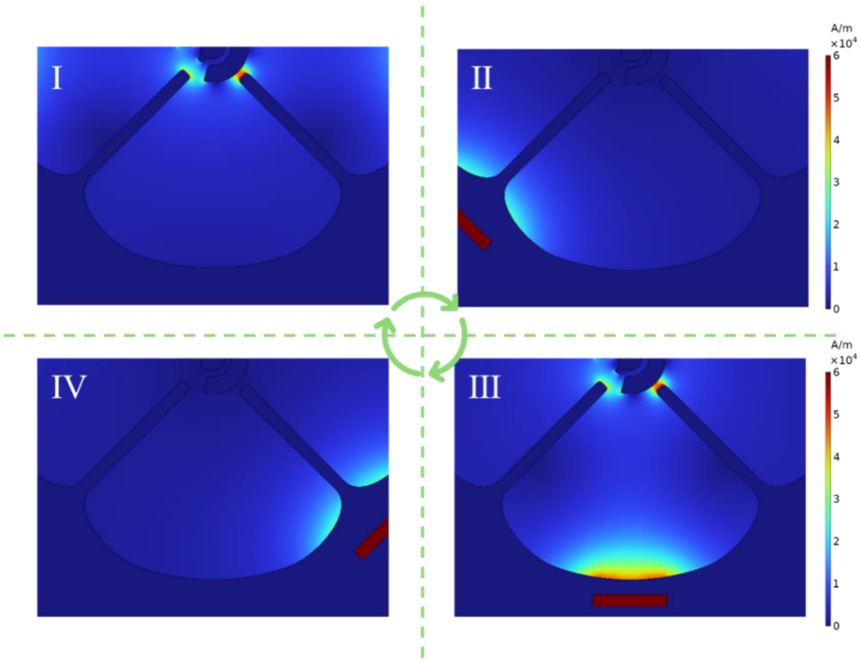

Figure S12. COMSOL simulation diagrams of magnetization intensity for the four working states of one set of friction layers of the FL-TENG during the rotation of the magnet.

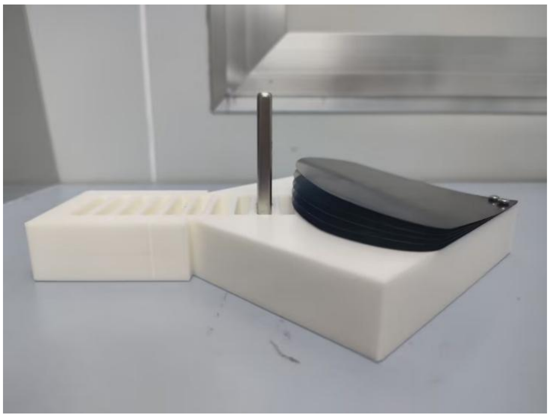

Figure S13. Test platform for friction layer separation at different horizontal distances. A total of five steel sheets were utilized. The magnets with dimensions of 50 mm × 30 mm × 5 mm were employed, and the vertical distance between the magnets and the friction layer (**Figure S20**) was set to -10 mm.

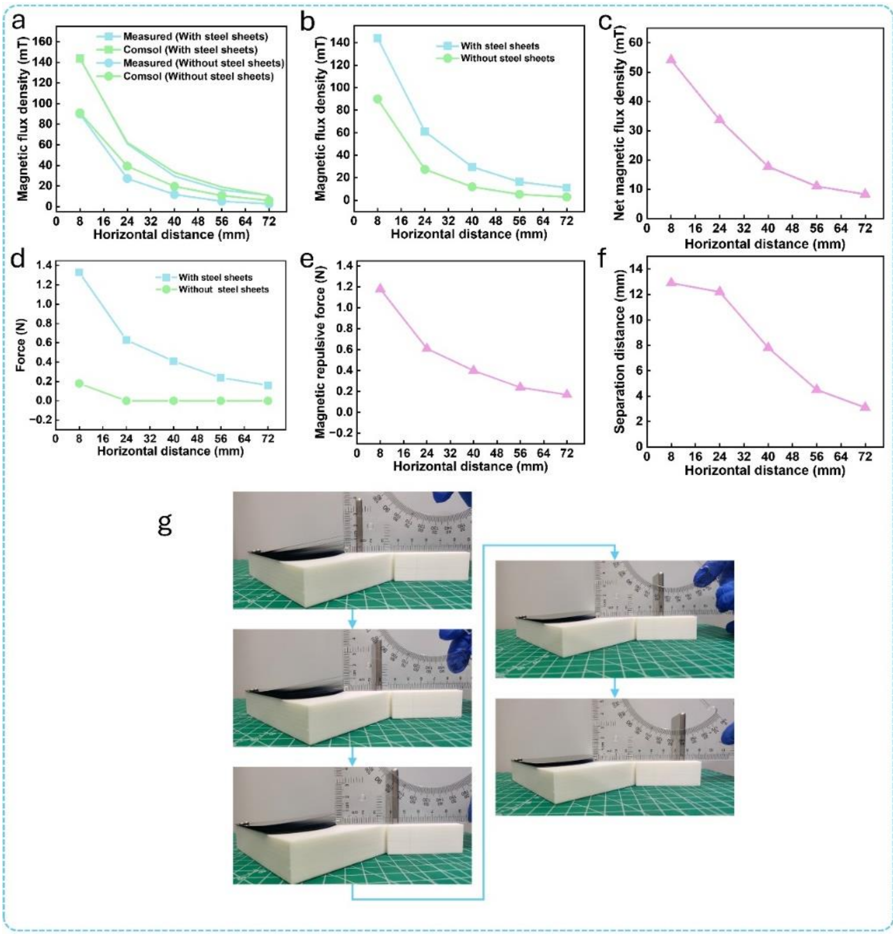

Figure S14. Test results for various parameters at different horizontal distances between the magnets and the Si-Mn steel friction layers. a: Comparison between experimental measurements and COMSOL simulations of magnetic flux density distribution along the horizontal direction, with and without steel sheets. b: Measured magnetic flux density near the center of the outer edge of the friction layers with and without Si–Mn steel sheets. c: Net magnetic flux density induced by magnetization of Si–Mn steel sheets derived from measured data of the two experimental groups. d: Forces measured by the tension gauge at the identical position, including the total force and the interference force exerted by the magnets on the measuring device in the absence of steel sheets. e: Interlayer magnetic repulsive force between the friction layers. f: Separation distance of the friction layers. g: Photographs showing the triboelectric layer separation at various horizontal distances.

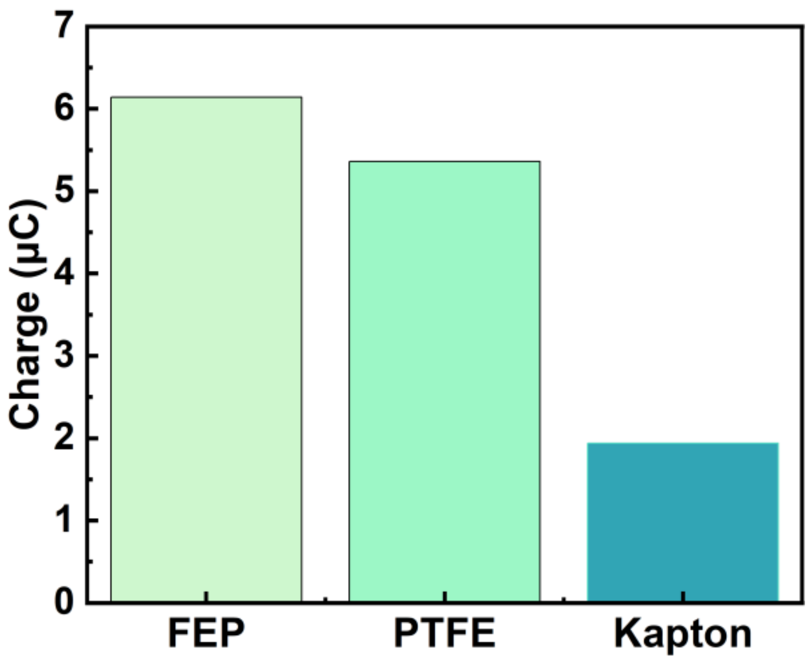

Figure S15. Comparison of transferred charge for different negative e friction layers ectrode materials of the FL-TENG based on the magnetic force separation principle mounted on a motor, under the conditions of 6 steel sheets and a rotational speed of 30 rpm.

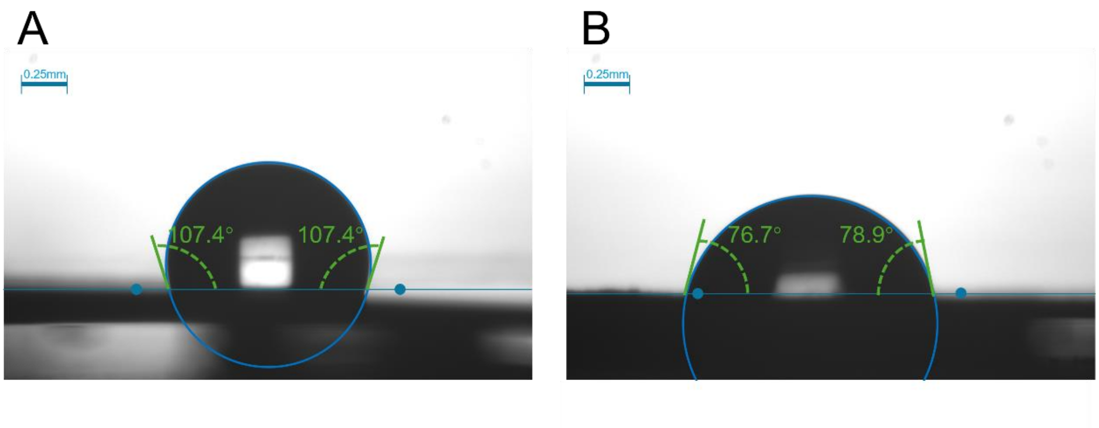

Figure S16. Static contact angles. (A) FEP and (B) silicon-manganese steel sheet.

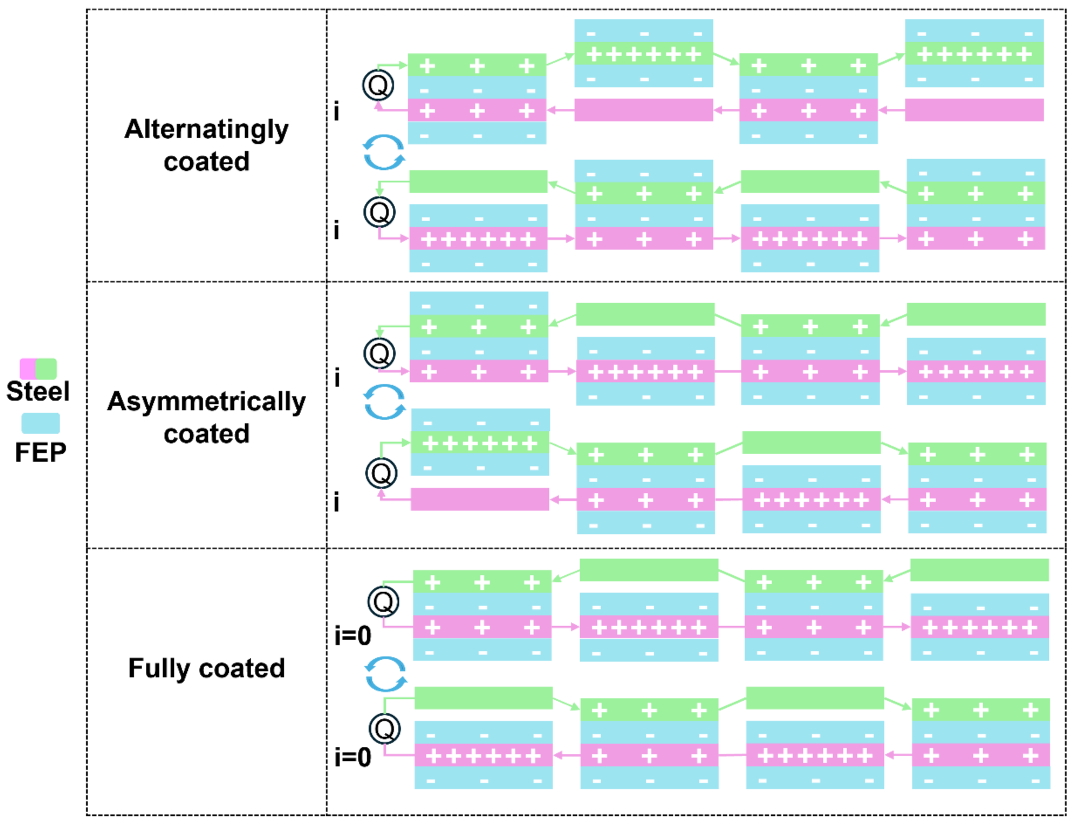

Figure S17. Comparison of working principles for three different coated methods.

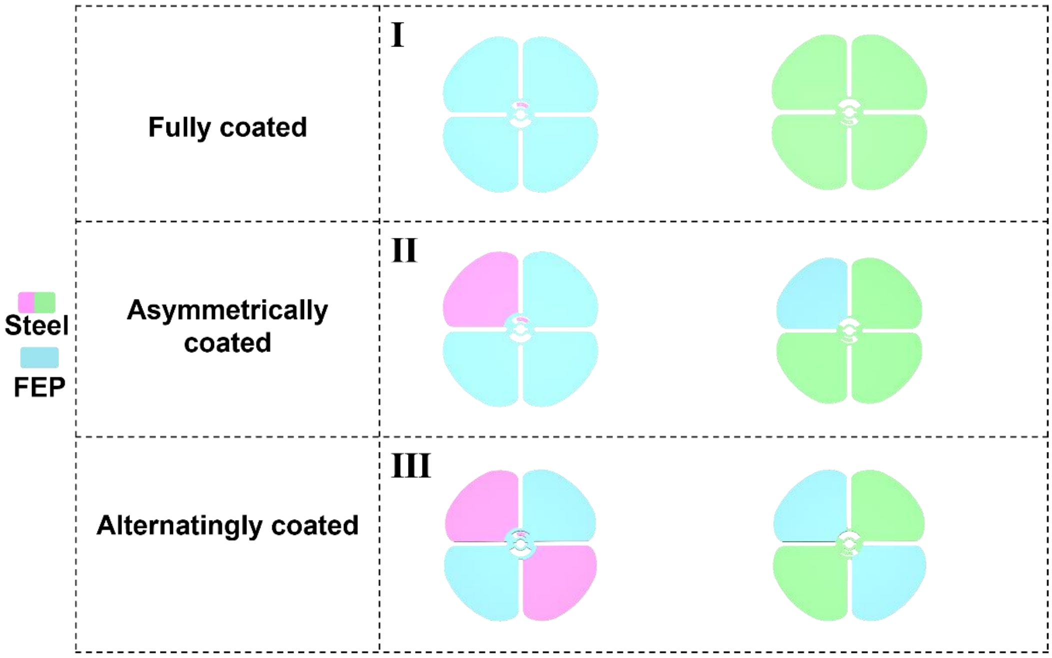

Figure S18. Three different coated methods of the four-leaf clover silicon-manganese steel sheets.

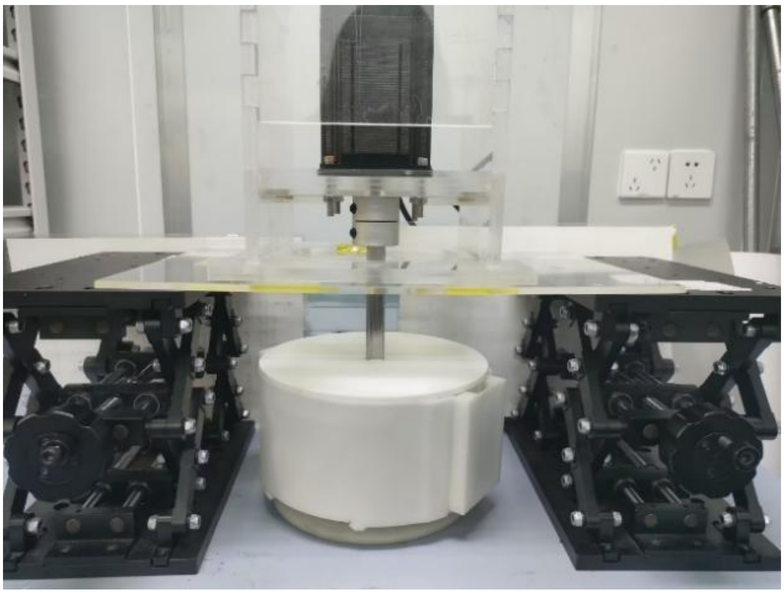

Figure S19. Photograph of the test platform.

Table S2. Orthogonal experimental table of the FL-TENG with nine different magnet dimensions and the corresponding short-circuit transferred charge, short-circuit current, and open-circuit voltage.

Experiment No.	Height (mm)	Width (mm)	Thickness (mm)	Charge (μC)	Current (μA)	Voltage (V)
1	40	10	10	10.04	91.00	169
2	40	20	3	3.90	31.01	63
3	40	30	5	12.82	143.13	216
4	50	10	5	3.81	27.81	63
5	50	20	10	11.54	109.69	211
6	50	30	3	8.41	86.79	136
7	60	10	3	1.02	8.75	17
8	60	20	5	11.41	105.97	189
9	60	30	10	11.29	80.25	211

Table S3. Data processing results of the FL-TENG with magnet height as the variable in the magnet dimension experiments.

Height (mm)	Charge (μC)	Current (μA)	Voltage (V)
40 ((No.1+ No.2+ No.3)/3)	8.92	88.38	149
50 ((No.4+ No.5+ No.6)/3)	7.92	74.76	137
60 ((No.7+ No.8+ No.9)/3)	7.91	64.99	139

Table S4. Data processing results of the FL-TENG with magnet width as the variable in the magnet dimension experiments.

Width (mm)	Charge (μC)	Current (μA)	Voltage (V)
10 ((No.1+ No.4+ No.7)/3)	4.95	42.52	83
20 ((No.2+ No.5+ No.8)/3)	8.95	82.22	154
30 ((No.3+ No.6+ No.9)/3)	10.84	103.39	188

Table S5. Data processing results of the FL-TENG with magnet thickness as the variable in the magnet dimension experiments.

Thickness (mm)	Charge (μC)	Current (μA)	Voltage (V)
3 ((No.2+ No.6+ No.7)/3)	4.44	42.18	72
5 ((No.3+ No.4+ No.8)/3)	9.35	92.30	156
10 ((No.1+ No.5+ No.9)/3)	10.96	93.65	197

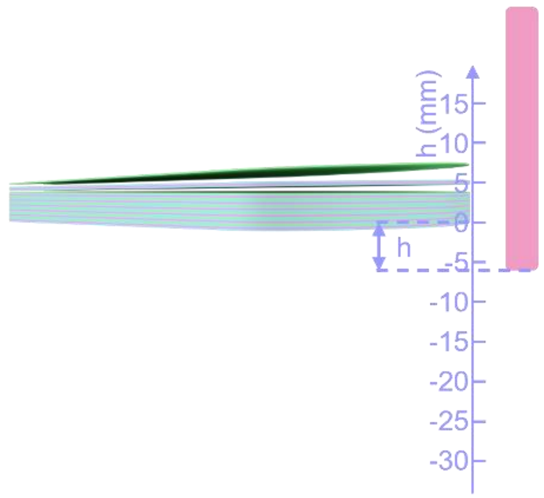

Figure S20. Schematic diagram of the vertical distance between the magnet and the FL-TENG.

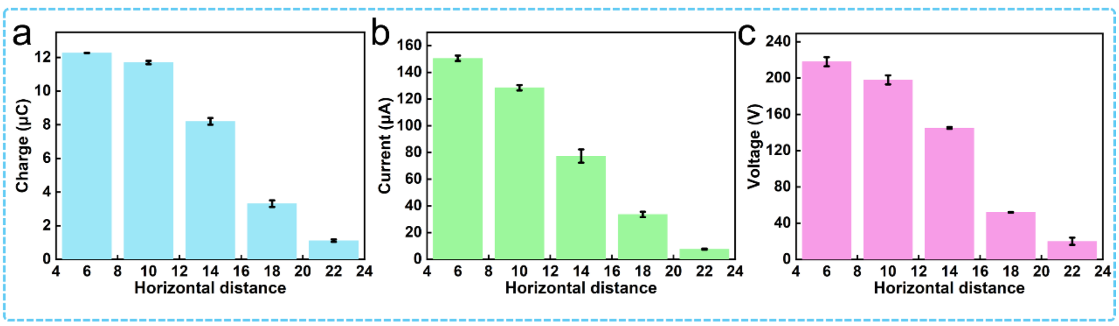

Figure S21. a: Transferred charge at different horizontal distances between the magnet and the triboelectric layer. b: Short-circuit current. c: Open-circuit voltage. Data are presented as mean values ± SD (n = 5).

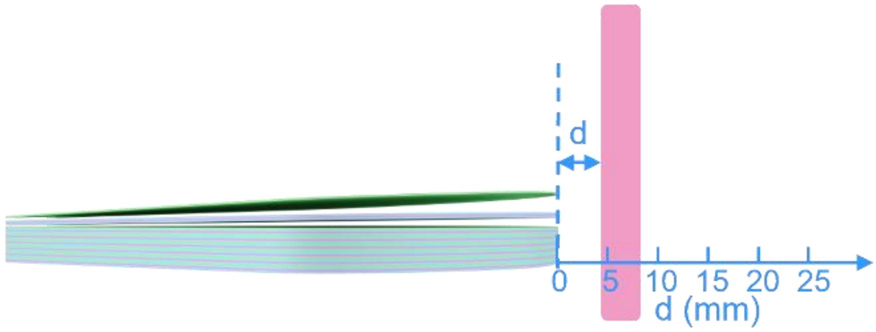

Figure S22. Schematic diagram of the horizontal distance between the magnet and the FL-TENG.

Note S1. The energy conversion efficiency of the FL-TENG.

To quantitatively characterize the energy conversion efficiency of the FL-TENG, an approximate estimation was carried out in this work by driving the device with a motor. The rotor of the FL-TENG is mainly composed of a shell and magnets mounted on both sides, with its mass concentrated at the outer edge. Therefore, the thin-walled ring model was adopted to calculate the moment of inertia, and its expression is given by:

$$I_1 = m_1 R_1^2 \qquad (1)$$

where m_1 represents the total mass of the shell and two magnets, and R_1 denotes the radius of the shell. During the motor-driven test, a solid cover is installed on the top of the shell, and the moment of inertia of this component is calculated using the homogeneous solid disc model and its expression is given by:

$$I_2 = \frac{1}{2} m_2 R_2^2 \qquad (2)$$

where m_2 is the mass of the cover, and R_2 stands for the radius of the cover. The stable rotational speed of the rotor driven by the motor is set as n=100 rpm, and the corresponding angular velocity is expressed as:

$$\omega = \frac{2\pi n}{60} \qquad (3)$$

When the rotor runs stably, the overall rotational kinetic energy is regarded as the total mechanical energy of the device within a single motion cycle:

$$E_{in} = \frac{1}{2}(I_1 + I_2)\omega^2 \tag{4}$$

At a rotational speed of 100 rpm, the rotation period of the rotor is expressed as:

$$T = \frac{60}{n} \tag{5}$$

At a rotational speed of 100 rpm, the output power under the optimal matched load is selected as the device's output power P_{out}. Accordingly, the electrical energy output of the device within a single rotation cycle can be expressed as:

$$E_{out} = P_{out}T \tag{6}$$

The energy conversion efficiency is defined as the ratio of the output electrical energy in a single cycle to the input rotational mechanical energy, and its expression is given by:

$$\eta = \frac{E_{out}}{E_{in}} \times 100\% \tag{7}$$

As shown in **Figure S23**, the total mass of the shell and two side magnets is m_1 = 0.6830 kg, and the mass of the cover is m_2 = 0.1595 kg. The geometric parameters are $R_1 = R_2 \approx 0.1$ m, and the output power under the optimal load is P_{out} = 22.25 mW. Substituting these parameters into the formulas yields an energy conversion efficiency of approximately 3.19%.

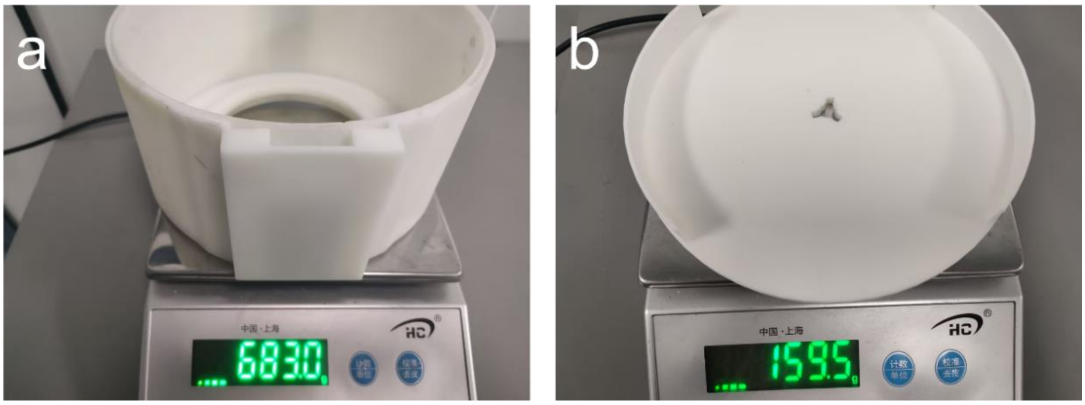

Figure S23: a: The total mass of the shell and two side magnets is m_1 = 0.6830 kg. b: The mass of the cover is m_2 = 0.1595 kg.

Table S6. Systematic comparison of rotary TENGs.

Starting wind speed (m/s)	**Transferred charge (μC)**	**Power density (W/m^3)**	**Energy conversion efficiency**	**Durability**	**Reference**
4	13.43	7.61	3.13%	98.71% in 1044 k (116 h)	This work
6.22	2.25	/	/	87.00% in 1200 k	Ref.[35]
2	1.72	/	/	95.70% in 271 k	Ref.[39]
13.1	0.12	3.43	12.68%	94.68% in 845 k	Ref.[40]
1.6	0.18	27.80		99.40% in 90 k	Ref.[41]
6	1.02	4.082	/	Around 97.00% in 54 k	Ref.[42]
1.7	6.77	0.056	/	Below 98.00% over 12.5 h	Ref.[43]

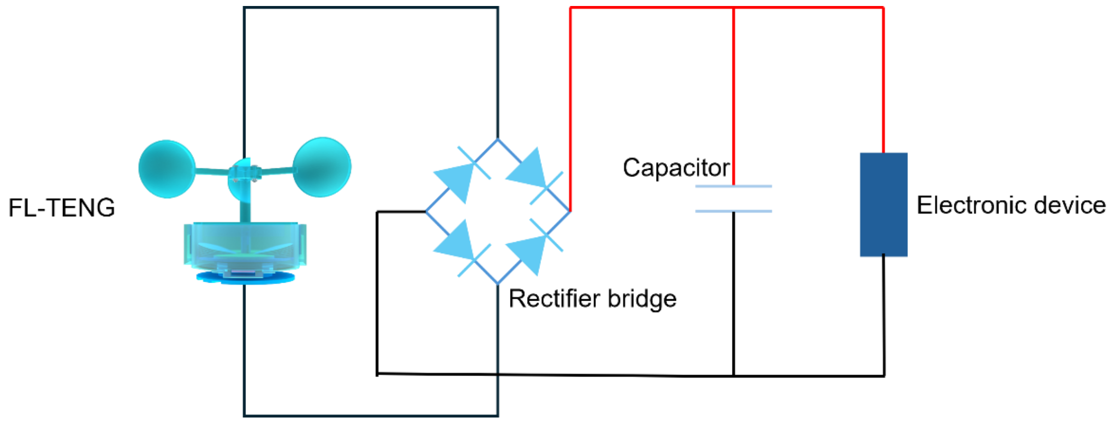

Figure S24. Schematic circuit diagram of the FL-TENG charging a capacitor after rectification.

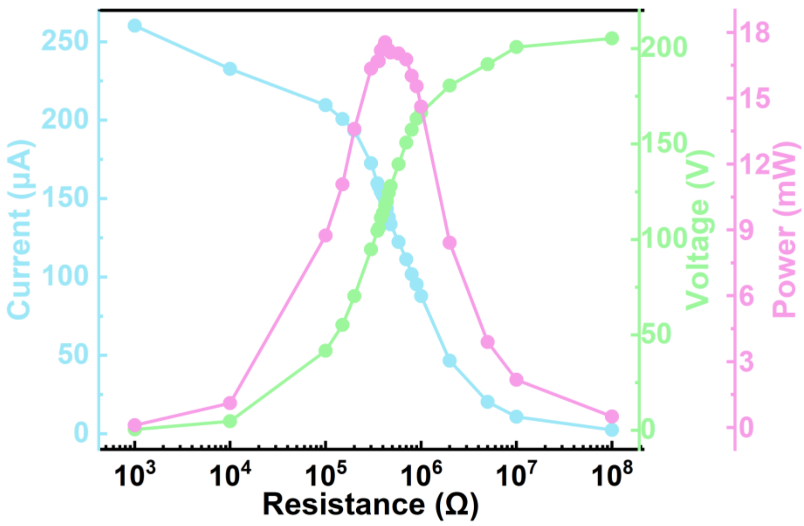

Figure S25. Output current, voltage, and instantaneous power under different external loads at 7 m/s.

List of Movies

Video S1. FL-TENG lit up the "GXU" logo composed of sixty-four series-connected LEDs.

Video S2. FL-TENG powered five parallel-connected calculators.

Video S3. FL-TENG powered twenty-five parallel-connected hygrothermographs.

Video S4. FL-TENG powered a multimeter.

Video S5. FL-TENG powered a flame sensor.